Research Article Vol. 9, No. 1 / January 2022 / Optica 71

Extreme-ultraviolet vector-vortex beams from high harmonic generation

Alba de las Heras,[1,5,†] Alok Kumar Pandey,[2,6,†] Julio San Román,[1] Javier Serrano,[1] Elsa Baynard,[2] Guillaume Dovillaire,[3] Moana Pittman,[2] Charles G. Durfee,[4] Luis Plaja,[1] Sophie Kazamias,[2] Olivier Guilbaud,[2] and Carlos Hernández-García[1]

[1]Grupo de Investigación en Aplicaciones del Láser y Fotónica, Departamento de Física Aplicada, Universidad de Salamanca, E-37008 Salamanca, Spain
[2]Laboratoire Irène Joliot-Curie, Université Paris-Saclay, UMR CNRS, Rue Ampère, Bâtiment 200, F-91898, Orsay Cedex, France
[3]Imagine Optic, 18, rue Charles de Gaulle, 91400 ORSAY, France
[4]Department of Physics, Colorado School of Mines, Golden, Colorado 80401, USA
[5]e-mail: albadelasheras@usal.es
[6]e-mail: alok-kumar.pandey@universite-paris-saclay.fr

Received 2 September 2021; revised 30 October 2021; accepted 15 November 2021; published 11 January 2022

Structured light in the short-wavelength regime opens exciting avenues for the study of ultrafast spin and electronic dynamics. Here, we demonstrate theoretically and experimentally the generation of vector-vortex beams (VVB) in the extreme ultraviolet through high-order harmonic generation (HHG). The up-conversion of VVB, which are spatially tailored in their spin and orbital angular momentum, is ruled by the conservation of the topological Pancharatnam charge in HHG. Despite the complex propagation of the driving beam, high-harmonic VVB are robustly generated with smooth propagation properties. Remarkably, we find out that the conversion efficiency of high-harmonic VVB increases with the driving topological charge. Our work opens the possibility to synthesize attosecond helical structures with spatially varying polarization, a unique tool to probe spatiotemporal dynamics in inhomogeneous media or polarization-dependent systems.

https://doi.org/10.1364/OPTICA.442304

1. INTRODUCTION

Advancing light engineering to structure the spatiotemporal properties of light beams is paramount to provide precise tools to explore fundamental material dynamics and to translate this knowledge into novel applications. Among the different kinds of structured beams [1], optical vortices and vector beams are consolidated as paradigmatic examples. While a vortex beam is spatially tailored in its phase, exhibiting a helical wavefront and thus carrying orbital angular momentum (OAM) [2,3], a vector beam is spatially tailored in its polarization state or spin angular momentum (SAM) [4,5]. Among all vector beam possibilities, radially and azimuthally polarized beams, exhibiting ordered linearly polarized distributions, are the most relevant examples. Harvesting the properties of vector and vortex beams has triggered substantial progress in many interdisciplinary fields such as optical communications [6–10], quantum information [11–13], topological systems [14,15], imaging [4,16–19], magnetism [20–23], material processing [24–26], optical tweezers [27–31], or particle acceleration [32,33]. In addition, structured light provides new scenarios of laser-matter interactions, like OAM transfer to valence electrons [34,35] and photoelectrons [36], or the control of electrical currents in a semiconductor [23,37].

Structured beams combining the spatial SAM distribution of vector beams with the helical phase of vortex beams have been generated in the infrared and visible spectral ranges [38–43]. These beams—referred to as vector-vortex beams (VVB)—exhibit complex dynamics during propagation, as they are not eigenmodes of the propagation operator. Noticeably, full Poincaré beams—containing all possible polarization states—can emerge upon the propagation of VVB [40,44]. In VVB, the characterization of OAM is nontrivial, as OAM arises both from the gradient of a twisted phase [2] as well as from the curl of the field polarization [45]. It is however possible to define a geometrical phase including both contributions—the Pancharatnam phase [46]—and the corresponding Pancharatnam topological charge, ℓ_P [38]. For a linearly polarized VVB, the OAM charge coincides with the topological Pancharatnam charge [38], but not in the general case [41,47].

While VVB have been generated in the visible-infrared (IR) regimes [38–43], their realization and characterization in the extreme ultraviolet (XUV)/x-ray spectral domains has not been addressed yet. The generation of such high-frequency coherent structured beams is desirable to achieve higher spatial and temporal resolutions, down to the nanometric and attosecond scales.

Recently, it has been shown that the challenge of manipulating XUV light to imprint SAM and OAM can be fulfilled via the up-conversion of intense structured IR light into high-frequency harmonics. The fundamental mechanism of high-order harmonic generation (HHG) is well understood in terms of a semiclassical three-step picture [48]: the IR driver triggers the tunnel ionization of an electron, which is afterward accelerated by the field, and finally recombines with the initial bound state, resulting in the emission of XUV attosecond bursts [49,50]. Thanks to the separate conservation of OAM and SAM in HHG, it has been demonstrated that infrared vortices, as well as vector beams, can be converted into the XUV [51–63]. Moreover, the synchronous control on both the polarization and the OAM is also possible via HHG, resulting in high harmonic beams carrying an averaged fractional OAM using conically refracted drivers [64], circularly polarized high-harmonic vortex beams [65–67], or time-ordered polarization states [68].

In this paper, we demonstrate experimentally and theoretically the generation and characterization of coherent XUV vector-vortex beams, merging their spatial phase and polarization distributions in a controllable fashion. Our results show the robust up-conversion of VVB from the IR to the XUV via HHG, with increasing efficiency for drivers with higher topological charges. The coupled conservation laws of SAM and OAM allow for the generation of radially or azimuthally polarized harmonic beams carrying high OAM, with smooth propagation properties, and emitted in the form of attosecond light-springs with radial or azimuthal polarization. Remarkably, we find that the topological charge of the XUV VVB—defined by the Pancharatnam phase—scales linearly with the harmonic order, in analogy with the selection rule for OAM in a pure vortex beam [51]. Finally, we also show that the intrinsic dipole phase introduced by the quantum paths during HHG imprints its signature as a tilt of the polarization direction in the harmonic VVB. The demonstration of VVB in the XUV opens new perspectives with the translation of the applications of conventional VVB beams to the short wavelength regime. In particular, the possibility of synthesizing XUV attosecond helical structures with spatially varying polarization constitutes a unique spatiotemporal feature that can be instrumental to probe spatiotemporal dynamics in inhomogeneous media or polarization-dependent systems, like anisotropic or chiral configurations.

2. METHODS

A. Experimental Setup

In Fig. 1, we depict the experimental setup to generate an XUV VVB from a linearly polarized Gaussian beam of central wavelength 815 nm, pulse duration ∼40 fs, ∼15 mJ maximum energy, and diameter of ∼24 mm at $1/e^2$. The IR vector-vortex driver with topological charge ℓ is obtained using a spiral phase plate and a polarization converter. The polarization converter is composed of eight half-waveplates where each octant has a different optical axis orientation. Note that the resulting configuration can be continuously tuned from radial to azimuthal by varying the polarization of the fundamental IR beam from vertical to horizontal. A 2-m focal length lens loosely focuses the resulting IR vector-vortex driving beam into a 15 mm long argon-filled gas cell to generate high harmonics. The distance between the polarization converter and the lens is ∼10 cm. After filtering out the residual IR driver with a 300 nm thick Al filter, the high-harmonic beam is guided to a high-resolution XUV Hartmann wavefront sensor (EUV-HASO, Imagine Optic) through a narrowband 45-degree multilayer flat mirror [69]. The flat mirror acts simultaneously as a spectral and a polarization filter, selecting the vertically polarized component of the 25th harmonic, centered at $\lambda_{XUV} = 32.6$ nm; the extinction of neighboring orders exceeds 90% [69], while the experimentally determined polarization selectivity is ∼10:1. Restricting the detection to a particular harmonic order allows for an unambiguous interpretation of the XUV vector-vortex wavefront. We use a spectral-phase control of the IR driver by an acousto-optic modulator (Dazzler, FASTLITE) to spectrally tune

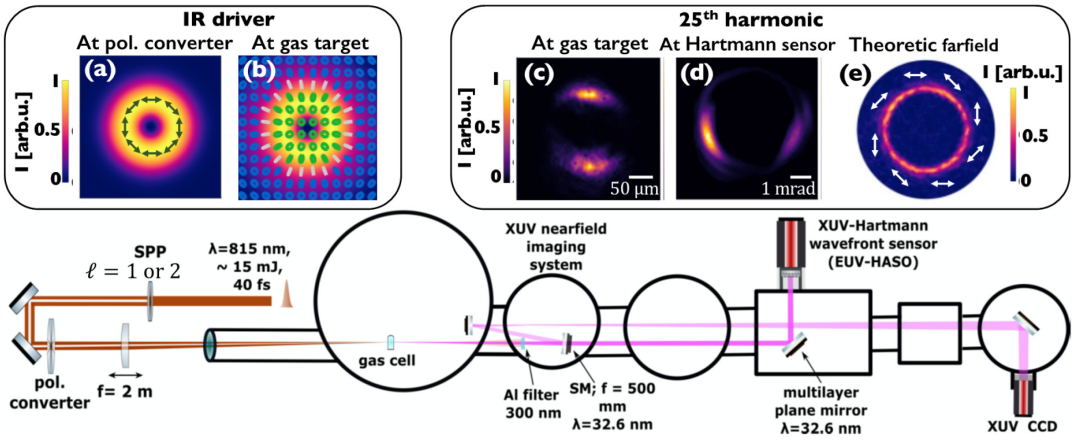

Fig. 1. Experimental setup for the generation of high-order harmonic VVB. A spiral phase plate (SPP) and a segmented polarization converter (pol. converter) are inserted into the incoming vertically-polarized IR Gaussian beam. The resulting IR vector-vortex is focused by a 2 m focal length lens into an argon gas cell. The remaining IR driver is removed using a 300 nm thick Al filter. The 25th harmonic of the driving beam centered at $\lambda_{XUV} = 32.6$ nm is spectrally selected using a 45° multilayer plane mirror and guided to the XUV Hartmann wavefront sensor (EUV-HASO) located ∼1.98 m from the source. The experimental setup is also equipped with an imaging system—comprising of a near-normal incidence concave mirror ($f = 500$ mm) and plane mirrors for beam steering—that allows for an intensity profile characterization of the HHG source and the attenuated IR beam at the focal plane. In the insets, we show the theoretical intensity and polarization distribution of the IR driver with total topological charge $\ell = 2$ at (a) the polarization converter and at (b) the gas target. We also depict the experimental vertical polarization component of the 25th harmonic beam (c) at the gas target and (d) at the far field, and (e) the corresponding simulation results of the harmonic far-field profile.

the high-harmonic beam. The experimental setup is also equipped with a high-magnification (∼6) monochromatic imaging system that allows for the intensity profile characterization of the beams at the gas cell: the HHG source and the attenuated IR beam at the focal plane.

Since VVB evolve during propagation, both the beam profile and the polarization structure are gradually modified from the polarization converter to the gas cell. As an example, the insets of Fig. 1 show the transformation of a VVB driver with $\ell = 2$ and its 25th harmonic beam. The azimuthally polarized IR driver right after the polarization converter [Fig. 1(a)] evolves into a full-Poincaré beam at the gas target [Fig. 1(b)]. High-order harmonics are generated with a radial polarization at the gas target [Fig. 1(c)], leading to nearly azimuthally polarized high-order harmonics in the far field [Figs. 1(d) and 1(e)]. The intrinsic dipole phase of each high-order harmonic causes a tilt of the polarization direction, which will be further discussed in Section 3.D.

B. Theoretical Approach

To simulate the nonlinear up-conversion of VVB, we model the HHG process both from the microscopic and macroscopic points of view. On the one hand, we use a combined model that considers a quantum description of HHG and takes into account propagation [70]. We compute the dipole acceleration of the target's argon atoms located at the focal plane using the quantum strong-field approximation (SFA), i.e., without resorting to the semiclassical saddle-point approximation. Note that for the parameters considered in this work, each atom perceives a locally homogeneous driving field. Then, the emitted harmonic field is propagated to the far-field detectors according to the electromagnetic field propagator [70]. This joint approach has been already corroborated against different experiments of structured HHG (see for example Refs. [62,63,66,71]). In this work, the spatial structure of the vector-vortex driver at the polarization converter plane is represented as a Laguerre-Gaussian mode

$$LG_{\ell,m}(\rho,\phi,z)\boldsymbol{e}_{\mathbf{p}} = E_0 \frac{W_0}{W(z)}\left(\frac{\rho}{W(z)}\right)^{|\ell|} L_m^{|\ell|}\left[\frac{2\rho^2}{W^2(z)}\right] \times \exp\left(-\frac{\rho^2}{W^2(z)}\right)\exp\left(-ik\frac{\rho^2}{2R(z)} + ig(z) - i\ell\phi\right)\boldsymbol{e}_{\mathbf{p}}, \tag{1}$$

with spatially varying polarization $\boldsymbol{e}_{\mathbf{p}} = \cos(\phi+\varphi_0)\boldsymbol{e}_{\boldsymbol{x}} + \sin(\phi+\varphi_0)\boldsymbol{e}_{\boldsymbol{y}}$. ϕ is the azimuthal coordinate, $L_m^{|\ell|}$ the generalized Laguerre polynomial, W_0 the beam waist, $z_R = \pi W_0^2/\lambda$ the Rayleigh length, $W(z) = W_0\sqrt{1+(z/z_R)^2}$ the beam width, $R(z) = z(1+(z_R/z)^2)$ the phase-front radius, $g(z) = (2m+|\ell|+1)\tan^{-1}(z/z_R)$ the Gouy phase, and $k = 2\pi/\lambda$ the wavenumber. The azimuthal index ℓ corresponds to the topological charge, and m is the radial index, which in this work is chosen to be $m = 0$. φ_0 is the parameter that determines the overall orientation of the polarization distribution. In particular, radial and azimuthal polarization distributions correspond to $\varphi_0 = 0$ and $\varphi_0 = \pi/2$, respectively.

To obtain the driving IR VVB distribution at the gas target, we compute the Fraunhofer diffraction integral along the transverse profile at the polarization converter, mimicking the experimental procedure. In all the simulations, we model the laser pulse with a central wavelength of $\lambda = 800$ nm and a sine-squared envelope with full width at half maximum (FWHM) in intensity of 15.4 fs. We chose a relatively shorter pulse duration (15.4 fs FWHM) compared to the experiment (40 fs FWHM) to reduce computational time, which, to the best of our knowledge, does not imply fundamental deviations in the results presented in this work. W_0 and the distance between the polarization converter and the gas target are chosen to achieve a beam size comparable to the experiment (see Fig. 2). This distance is just a scaling factor of the beam size without influencing any other attributes of the driving beam. In this work, we consider driving VVB with topological charges of $\ell = 1$ and $\ell = 2$, for which the peak intensities at the gas target are 9.7×10^{14} and 3.2×10^{14} W/cm^2, respectively.

On the other hand, we use the thin slab model (TSM) [52,56] to analyze the role of the intrinsic dipole phase in the generation of XUV VVB from HHG. The TSM is based on calculating the Fraunhofer diffraction of the high-order harmonics generated at the gas, which is approximated following strong-field assumptions. In this work, we have adapted the TSM description (see Ref. [56]) to take into account the decrease of the harmonic yield with the drivers' ellipticity by considering a mask function of the ellipticity ε (Ref. [72]). Thus, the harmonic field at the gas cell can be written as

$$A_q^j(\rho,\phi) = \left(\frac{1-\varepsilon^2}{1+\varepsilon^2}\right)^{\frac{q-1}{2}}\left(\frac{C}{\tau^j}\right)^{3/2}|U(\rho,\phi)|^{3.4} \times e^{iq\Phi(\rho,\phi)}e^{i\alpha_q^j|U(\rho,\phi)|^2}, \tag{2}$$

where q is the harmonic order, j is the index of the quantum path (short or long), α_q^j is the coefficient describing the intrinsic dipole phase of the quantum path, τ^j is the excursion time [73], $|U(\rho,\phi)|$ and $\Phi(\rho,\phi)$ are the driving amplitude and phase, and C is a constant. The short-trajectory coefficient in the intrinsic phase is set to $\alpha_q^s = 4.93 \times 10^{-14}$cm^2/W. Long trajectories ($\alpha_q^l = 2.03 \times 10^{-13}$cm^2/W) do not lead to efficient harmonic phase matching in this case, and thus their contribution is negligible. Finally, the harmonic field is projected on horizontal and vertical polarizations and propagated to the detectors with the Fraunhofer diffraction integral.

3. RESULTS

A. Driving IR Vector-Vortex Beam Characterization

The analysis of the driving field properties is paramount for interpreting the results from HHG and for deriving the conservation laws governing the up-conversion process. A VVB built from a vortex beam with OAM charge ℓ can be interpreted as a superposition of two vortex beams with counterrotating circular polarization (right circular RCP and left circular LCP), carrying topological charges $\ell_{\mathrm{RCP}} = \ell + 1$ and $\ell_{\mathrm{LCP}} = \ell - 1$, with a phase difference of $\varphi = (\varphi_{\mathrm{LCP}} - \varphi_{\mathrm{RCP}})/2$:

$$e^{-i\ell\phi}\left[\cos(\phi+\varphi)\boldsymbol{e}_{\boldsymbol{x}} + \sin(\phi+\varphi)\boldsymbol{e}_{\boldsymbol{y}}\right] = \left[e^{-i(\ell+1)\phi}\left(\boldsymbol{e}_{\boldsymbol{x}} + i\boldsymbol{e}_{\boldsymbol{y}}\right) + e^{-i(\ell-1)\phi}e^{i2\varphi}\left(\boldsymbol{e}_{\boldsymbol{x}} - i\boldsymbol{e}_{\boldsymbol{y}}\right)\right]\frac{e^{-i\varphi}}{2}. \tag{3}$$

The inspection of Eq. (3) points out that the orientation of the polarization structure is governed by the phase shift 2φ between the LCP and RCP components. We also note that the LCP and RCP components are pure vortex beams with a different OAM

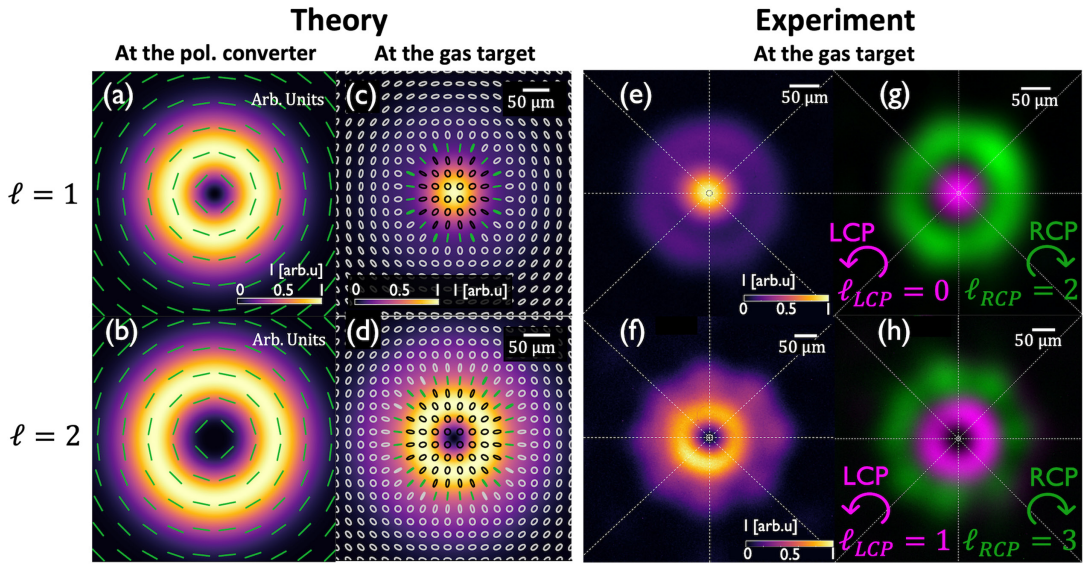

Fig. 2. Theoretical and experimental characterization of the IR vector-vortex driver for two topological charges: $\ell = 1$ (top row) and $\ell = 2$ (bottom row). The theory panel shows the intensity (colored background) and ellipticity (superimposed ellipses) profiles at (a), (b) the polarization converter plane and (c), (d) upon propagation to the gas target. In the experimental panel, we show the (e), (f) intensity profile of the total beam and (g), (h) its decomposition on right and left circular polarization (RCP and LCP). Note that the clean input beam with linear azimuthal polarization transforms into a complex radial structure at the gas target.

charge. However, the topology of a VVB is characterized by the Pancharatnam phase [38], which establishes a relation between the phases of two distinct polarization states [46]. The Pancharatnam phase is defined as the argument of the inner product of two polarized waves. Since we can write the total field as $|E\rangle = A_R e^{-i(\ell+1)\phi}|\mathrm{RCP}\rangle + A_L e^{-i(\ell-1)\phi} e^{i2\varphi}|\mathrm{LCP}\rangle$, the Pancharatnam phase is

$$\begin{aligned}\varphi_P &\equiv -\mathrm{Arg}(\langle E(\phi=0)|E\rangle)\\ &= \ell\phi + \tan^{-1}\left(\frac{|A_R|^2 - |A_L|^2}{|A_R|^2 + |A_L|^2}\tan(\phi)\right),\end{aligned} \tag{4}$$

where $|E(\phi=0)\rangle$ is the reference field. The first term is equal to the azimuthal phase of a scalar vortex, whereas the second term is nonvanishing in nonlinear polarization patterns [41]. By applying the definition of the topological Pancharatnam charge, ℓ_P, (Ref. [38]), we obtain

$$\ell_P \equiv \frac{1}{2\pi}\oint_C \varphi_P = \ell = \frac{\ell_{\mathrm{RCP}} + \ell_{\mathrm{LCP}}}{2}, \tag{5}$$

where the second term of the Pancharatnam phase cancels along the closed path C encircling the central singularity. Thus, the topological Pancharatnam charge ℓ_P of the VVB equals the OAM charge ℓ of the vortex beam used to build the VVB (i.e., before arriving at the polarization converter in Fig. 1), which coincides with the average of the topological charge of the RCP and LCP modes.

We remark that a VVB is not an eigenmode of the propagation operator and thus, the polarization state along propagation depends on the change of the relative phase and divergence properties of each RCP and LCP vortex beam. Assuming these vortex beams as Laguerre-Gaussian modes, their phase difference acquired during propagation is due to the Gouy phase

$$\Delta g(z) = (|\ell_{\mathrm{LCP}}| - |\ell_{\mathrm{RCP}}|)\tan^{-1}(z/z_R). \tag{6}$$

Hence, the orientation of the polarization structure changes along the propagation axis according to $\varphi(z) = \varphi_0 + \Delta g(z)/2$, where φ_0 is the orientation parameter of the polarization pattern at the waist. The rotation of the polarization plane upon propagation can be levorotatory ($|\ell_{\mathrm{LCP}}| > |\ell_{\mathrm{RCP}}|$) or dextrorotatory ($|\ell_{\mathrm{RCP}}| > |\ell_{\mathrm{LCP}}|$). This intrinsic property of VVB can be interpreted as an axially-dependent optical activity [39,42,43], in analogy with the circular birefringence present in chiral media. In particular, the polarization of a radial (azimuthal) VVB at the waist rotates to azimuthal (radial) in the far field, since the accumulated phase shift between LCP and RCP modes is $\pm\pi$. Note that in the case of a pure vector beam ($\ell = 0$) or a pure vortex beam ($\ell_{\mathrm{RCP}} = \ell_{\mathrm{LCP}}$) there is no phase shift, and consequently, no polarization rotation.

On the other hand, the divergence of a Laguerre-Gaussian mode depends on the topological charge through $|\ell|$ [see Eq. (1)]. Therefore, the structure of a VVB—exhibiting $\ell_P = \ell \neq 0$—is not preserved upon propagation, due to the different divergences of the LCP and RCP modes. The different divergences of the two modes lead to an axially dependent distribution of the total beam, covering exotic polarization structures like a full-Poincaré beam [40,44]. In our HHG setup, while the driving VVB polarization states occupy the equator of the Poincaré sphere at the polarization converter plane, the polarization distribution evolves to span the entire Poincaré sphere at the gas target.

In Fig. 2, we show the results of the theoretical and experimental characterization of the IR driving intensity and ellipticity for a VVB with topological charge $\ell = 1$ (top row) and $\ell = 2$ (bottom row). The left panel [Figs. 2(a)–(d)] displays the intensity profile together with the local polarization ellipses at (a), (b) the polarization converter plane and (c), (d) upon propagation to the gas target. Though the IR beam presents a clean structure with linear polarization right after the polarization converter, the complex distribution of a full-Poincaré beam arises at the target, as shown in (c), (d) theory and (e), (f) as retrieved from the experiments. By filtering the RCP or LCP components (g), (h), we can distinguish

experimentally the two vortex beams with distinct topological charges and opposite polarization helicity ($\ell_{RCP} = 2$ and $\ell_{LCP} = 0$ for $\ell = 1$, and $\ell_{RCP} = 3$ and $\ell_{LCP} = 1$ for $\ell = 2$) that compose the total beam. The RCP and LCP components are separated using a combination of a quarter-waveplate and a linear polarizer placed in between the polarization converter and the focusing lens, hence allowing us to identify the handedness of each circularly polarized component. The radii of maximum intensity of the separated beams are in agreement with the expected OAM charges, ℓ_{RCP} and ℓ_{LCP}, for each component [74]. The spatial region where the two modes overlap with the same intensity conforms to a ring of linear polarization (null ellipticity, green straight lines), whereas smaller (bigger) radius correspond to (c), (d) left-handed (right-handed) ellipticities represented with black (white) ellipses. Moreover, we note that the polarization distribution of the driving beam evolves from azimuthal at the converter plane to radial at the gas target, due to the Gouy phase shift.

B. Generation and Characterization of Harmonic VVB

Despite the complex structure of the driving field at the target, high-order harmonics with robust vector-vortex conformations are observed in the harmonic far field. Figure 3 shows the vertical polarization intensity projection (top) and the wavefront (bottom) of the 25th harmonic in the far field for the vector-vortex drivers presented in Fig. 2, with topological charges $\ell = 1$ (left) and $\ell = 2$ (right). The 25th harmonic exhibits a wavefront that twists with $\ell_{25} = 25$ [Fig. 3(b)] for the $\ell = 1$ driver and with $\ell_{25} = 50$ for the $\ell = 2$ driver [Fig. 3(d)]. The resulting Pancharatnam topological charge of the q-th harmonic order VVB scales linearly with the Pancharatnam topological charge of the driving VVB, i.e., $\ell_{Pq} = q\ell_P$, in analogy to the scaling law found for a vortex beam with a homogeneous polarization [51]. We anticipate that this is not a trivial result, as the linear conservation law applies to the VVB Pancharatnam topological charge, and not to the OAM contributions of the modes that compose the VVB, as we will discuss later. In addition, the vertical polarization component of the far-field harmonic [Figs. 3(a) and 3(c)] presents the typical structure of an azimuthal vector beam but shifted by a certain angle due to the intrinsic dipole phase, whose origin will be also discussed later. We attribute the slight differences between the theoretical and experimental harmonic intensity profiles to the differences in their driving beam profiles (Fig. 2), and to small deviations in the estimation of the driving peak intensities.

The propagation behavior of VVB, together with the nature of HHG, imply that the properties of the driving IR VVB are not always directly mapped into the high-order harmonics. In particular, the inhomogeneous ellipticity distribution of the VVB at the gas target restricts HHG to specific spatial regions, since only low ellipticities lead to efficient high-order harmonic emission [72,75,76]. Such constraint implies that the HHG process circumvents the complex full-Poincaré beam at the target, selecting regions with nearly linear polarization. As a consequence, high-order harmonics result in a cleaner polarization structure at the gas target [see Fig. 1(c)].

The harmonic build-up must be interpreted from the point of view of the simultaneous conservation of OAM and SAM. In the photon picture, one should consider the combination of photons of the driving LCP and RCP modes, a situation similar to HHG driven by conical refraction beams [64]. Energy conservation establishes that for the q-th harmonic order, $q = n_{RCP} + n_{LCP}$ (being n_{RCP} and n_{LCP} the number of RCP and LCP absorbed photons, respectively). Since the symmetry of the driving field and the atomic element restricts q to an odd integer, there are two equally probable channels satisfying SAM conservation, i.e., $n_{RCP} - n_{LCP} = \pm 1$ [77]. Thus, SAM and energy conservation dictate that $(n_{RCP} = \frac{q+1}{2}, n_{LCP} = \frac{q-1}{2})$ is the RCP channel, and $(n_{RCP} = \frac{q-1}{2}, n_{LCP} = \frac{q+1}{2})$ is the LCP channel. Therefore, OAM conservation of each separate channel $\ell_{q,\mathrm{RCP\,or\,LCP}} = n_{RCP}(\ell + 1) + n_{LCP}(\ell - 1)$ results in $(\ell_{q,RCP} = q\ell + 1, \ell_{q,LCP} = q\ell - 1)$, which allows for the generation of radially or azimuthally polarized harmonic beams carrying OAM. This simultaneous conservation law can be observed in Fig. 4, where we present the calculated topological charge spectra for several far-field harmonic orders, decomposed in RCP and LCP for a vector-vortex driver with $\ell = 2$ bearing azimuthal polarization right after the polarization converter. We calculate the topological charge by computing the Fourier transform of a certain polarization component along the azimuthal coordinate. The qth-order harmonic results from the superposition of $\ell_{q,RCP} = q\ell + 1$ and $\ell_{q,LCP} = q\ell - 1$ modes, leading to a VVB with Pancharatnam topological charge $\ell_{Pq} = q\ell_P$. In the inset of Fig. 4, we zoom out the 25th harmonic to highlight the topological charge of each

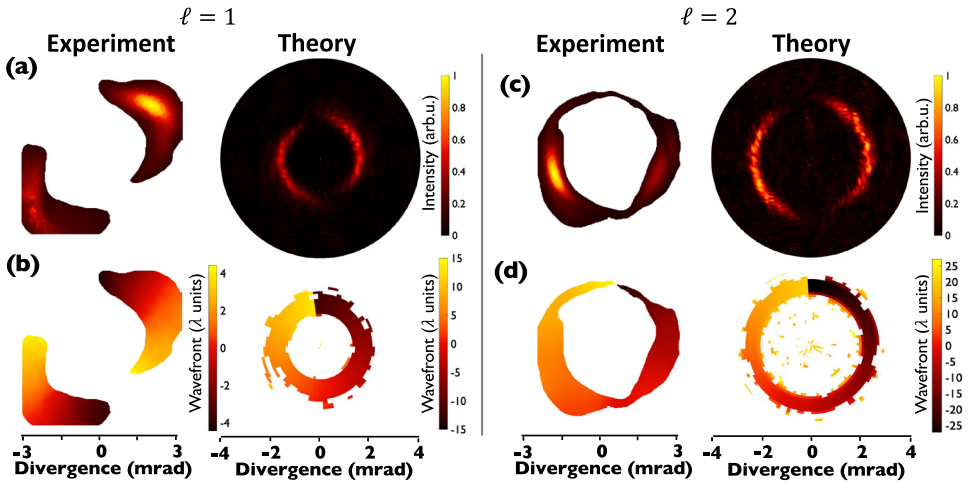

Fig. 3. Characterization of the 25th harmonic in the far field for the vector-vortex drivers with topological charge (a), (b) $\ell = 1$ and (c), (d) $\ell = 2$ shown in Fig. 2. We compare the experimental measurements and numerical results of the vertical polarization intensity projection and the wavefront.

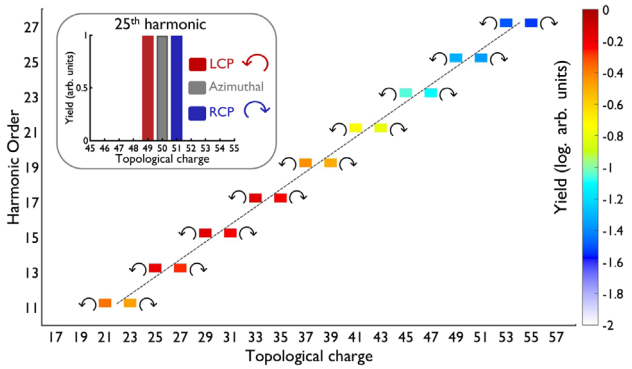

Fig. 4. Conservation law of SAM and OAM in HHG driven by a vector-vortex beam with topological charge $\ell = 2$ and generated with azimuthal polarization at the polarization converter. Each harmonic order, q, is a superposition of two circularly polarized modes (RCP and LCP) with $\ell_{q,\mathrm{RCP}} = q\ell + 1$ and a $\ell_{q,\mathrm{LCP}} = q\ell - 1$, which results in a net topological charge $\ell_q = q\ell$. In the inset, we zoom out the 25th harmonic to emphasize the topological charge of each polarization component.

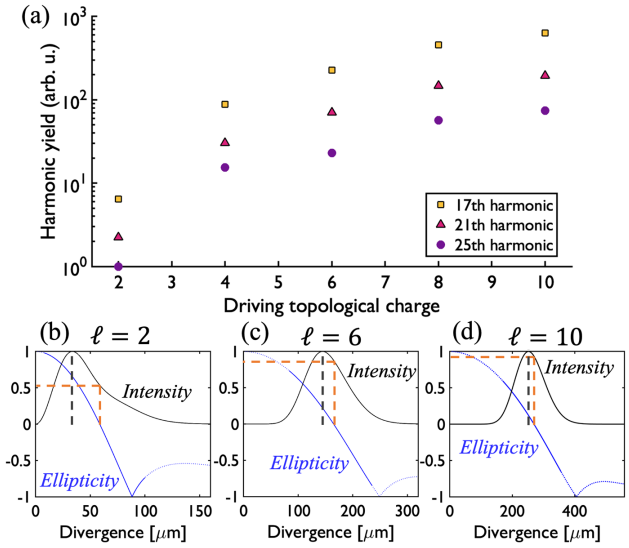

Fig. 5. (a) The efficiency of HHG increases for vector-vortex drivers with higher topological charge, until saturation. At the bottom row of the figure, we show the driving intensity profile (black solid line) and ellipticity (blue solid line) at the gas target for different topological charges: (b) $\ell = 2$, (c) $\ell = 6$ and (d) $\ell = 10$, while keeping constant the radius at the polarization converter and a peak intensity of 2×10^{14} W/cm^2 at the gas target. Drivers with higher topological charge produce a better overlap of the right and left circular components, leading to a larger region of nearly null ellipticity (linear polarization, orange dashed line) that approaches the radius of peak intensity (black dashed line).

polarization component. For the case presented, the topological charge of the azimuthal polarization is $\ell_{25} = 50$, in agreement with the experimental wavefront measurement in Fig. 3(d). Since the harmonic beam exhibits an azimuthal polarization distribution in the far field, by computing the topological charge of this polarization we obtain the topological charge of the harmonic VVB, which coincides with the topological Pancharatnam charge.

These conservation laws imply that high-order harmonics are emitted with large OAM, and a constant topological charge difference between the counter-rotating polarizations, i.e., $\ell_{q,\mathrm{RCP}} - \ell_{q,\mathrm{LCP}} = 2$. This has bifold implications: (1) the phase shift introduced by the Gouy phase is the same for the fundamental driver and the high-order harmonics and thus, there is a synchronous polarization rotation from radial to azimuthal along the propagation axis; and (2) each high-harmonic beam integrates two high OAM modes with comparable divergence, and thus the propagation of the harmonic VVB is robust.

C. Scaling of the High-Harmonic Efficiency

We experimentally observed that a larger number of laser-shots were needed to obtain XUV Hartmanngrams with a high signal-to-noise ratio for the IR VVB of lower topological charge (100 shots for $\ell = 1$ and 30 shots for $\ell = 2$). This suggests a nontrivial relation between the IR VVB topological charge and the HHG efficiency. To understand this aspect, we have computed the yield of different harmonic orders as a function of the driving topological charge, ℓ. Our numerical results, [see Fig. 5(a)], show that the harmonic yield increases substantially with ℓ, until saturation. To understand it, we show the driving beam intensity profile (black solid line) and ellipticity (blue solid line) at the gas target for three cases: $\ell = 2$ [Fig. 5(b)], $\ell = 6$ [Fig. 5(c)], and $\ell = 10$ [Fig. 5(d)]. To perform a fair comparison, we have kept constant the beam radius at the polarization converter, and a peak intensity of 2×10^{14} W/cm^2 at the gas target. These figures show that the radius of linear polarization (null ellipticity, orange dashed line), where HHG is mainly produced, approaches the radius of peak intensity (black dashed line) for drivers with higher ℓ. In addition, the slope of the ellipticity flattens for drivers with a higher VVB topological charge. Consequently, the enhancement for high ℓ drivers is both due to the coincidence of the beam radii of low ellipticities with that of higher intensities, and the progressively thicker region with low ellipticities in the focal plane. The reason for this is that the RCP and LCP modes of the driving beam exhibit a better overlap for high ℓ values. The propagation of high OAM modes is much more alike and thus, a saturation regime of good overlap is justified.

D. Effect of the Intrinsic Dipole Phase and Attosecond Spatiotemporal Structure

We show in Fig. 6(a) the simulation results of the far-field vertical polarization component of the 25th harmonic driven by an azimuthal VVB with topological charge $\ell = 2$ in different theoretical models: TSM neglecting the intrinsic phase (left), TSM with the intrinsic phase of short trajectories (center) and the total quantum SFA calculation including propagation (right). Note that the noisy pattern present in the latter case [and also in Figs. 2(a) and 2(c)] is a numerical artifact that would disappear if a sufficiently large amount of single-atom SFA calculations were computed. Apart from the polarization rotation due to the Gouy phase, an additional polarization shift emerges only when the intrinsic phase is included in the calculations. In other words, a measurement of the polarization tilt of the harmonic VVB contains information about the intrinsic phase of short trajectory contributions, in this case. As a consequence, the intrinsic phase of HHG could be retrieved through ellipsometry measurements in the generation of harmonic VVB, similarly to the recent demonstration in noncollinear HHG [71]. The tilt of the polarization orientation is directly related to the dephasing between RCP and LCP modes according to Eq. (3). Since the accumulated phase on the electron quantum path strongly depends on the intensity, the radial intensity distribution at the target [see Figs. 2(c)–2(f)] is mapped

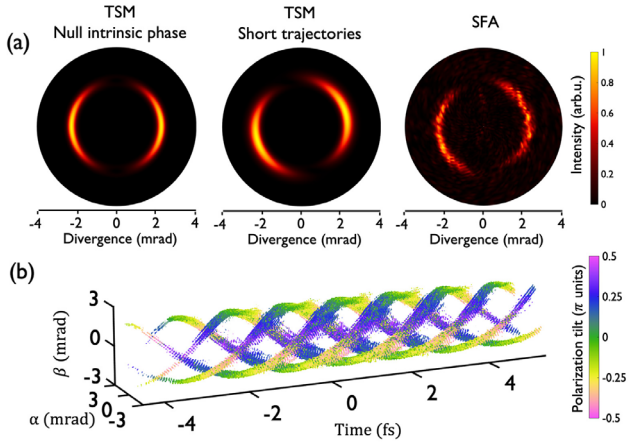

Fig. 6. (a) Far-field vertical polarization intensity of the 25th harmonic driven by an azimuthal vector-vortex of $\ell = 2$ in the different theoretical models: TSM neglecting the intrinsic phase (left), TSM with the intrinsic phase of short trajectories (center), and the full quantum SFA calculation (right). A spatial polarization shift emerges only when the intrinsic phase is included. (b) Helical spatiotemporal structure with azimuthal polarization resulting from the SFA calculation.

on the radial distribution of the intrinsic phase. Hence, the RCP mode occupying the outermost radius discerns higher values of the intrinsic phase than the LCP mode occupying the inner radius. Upon propagation to the far field, this dephasing results in a tilt of the polarization structure. This effect is relatively more significant for VVB drivers with low topological charge (comparing $\ell = 1$ and $\ell = 2$ in Fig. 3) because they exhibit a greater intensity gradient at the gas target [see Figs. 5(b)–5(d)]. We note that the comparison between theory and experiment in Fig. 3 does not allow to precisely extract this additional polarization tilt from the experimental results, and we attribute it to slight differences between the theoretical and experimental driving beam intensities.

The intrinsic phase is different for each harmonic order and therefore, each harmonic beam presents a slightly different tilt. Even so, by filtering harmonics beyond the 11th order, it is possible to obtain an attosecond light-spring with radial or azimuthal polarization. We show in Fig. 6(b) the spatiotemporal intensity and polarization tilt distribution of the attosecond pulses resulting from our full quantum calculations including propagation for an azimuthal vector-vortex driver with topological charge $\ell = 2$. In HHG, the linear scaling of both the frequency and the OAM with the harmonic order leads to helical dispositions—known as light-springs—in the spatiotemporal domain [51,78]. Remarkably, results in Fig. 6(b) demonstrate that we can also tailor the light-springs with an inhomogeneous polarization, providing a new degree of freedom in attosecond beams.

4. DISCUSSION

We demonstrate the up-conversion of VVB from the IR to the XUV on the grounds of high harmonic generation. The experimental and numerical characterization evidence that both the IR and XUV VVB combine the twisted phase of vortex beams with the inhomogeneous polarization structure of vector beams. By defining the topological charge of VVB through the geometrical Pancharatnam phase, we find out that this topological charge scales linearly with the harmonic order in HHG. Interestingly, we obtain an increase of the HHG efficiency for drivers with a higher topological charge, so this scheme allows for an efficient generation of high-charge VVB. By filtering the high-harmonic orders, we harness a helical attosecond structure with a spatially varying polarization that can conform to radial or azimuthal configurations. These XUV structured beams combining phase and polarization singularities can reveal new insights into light-matter interactions in semiconductors, magnetic or topological materials, and enable substantial advances in high-resolution imaging [79] or high-capacity optical communications, among other fields.

Additionally, we discern that the intricate behavior of non-pure driving modes of propagation is not directly mapped into the harmonic beam due to intrinsic features of HHG, such as the severe ellipticity dependence of HHG efficiency or the symmetries imposed by the conservation laws. In the up-conversion of VVB, HHG favors simpler spatially varying polarization distributions of the harmonic beam and smooth propagation effects towards the far field, without losing the essential characteristics of the driving beam. The harmonic VVB retains the levorotatory or dextrorotatory polarization along propagation, which can be a useful tool to probe chirality-sensitive processes or optical activity with high temporal and spatial resolution. Furthermore, we identify a tilt on the polarization direction of the harmonic beam as a signature of the nonperturbative phase of HHG, suggesting an indirect method to retrieve the intrinsic dipole phase accumulated along the electron quantum paths.

Funding. European Research Council (851201); Ministerio de Ciencia de Innovación y Universidades, Agencia Estatal de Investigación and European Social Fund (PID2019-106910GB-I00, RYC-2017-22745); Junta de Castilla y León and FEDER Funds (SA287P18); Université Paris-Saclay (2012-0333T-OASIS, 50110000724-OPTX, PhOM REC-2019-074-MAOHAm); Conseil Régional, Île-de-France (501100003990); Barcelona Supercomputing Center (FI-2020-3-0013).

Acknowledgment. The project leading to this publication has received funding from the ERC under the European Union's Horizon 2020 research and innovation program (ATTOSTRUCTURA - grant agreement No 851201). We acknowledge the computer resources at MareNostrum and the technical support provided by Barcelona Supercomputing Center (FI-2020-3-0013). The authors thank CEMOX installation at IOGS, Palaiseau, France, for the design and fabrication of the multilayer optics. We acknowledge the technical support of IJC Lab staff J. Demailly and O. Neveu. We are thankful to F. Quéré (Institut rayonnements matière du CEA, Saclay) for providing the polarization converter used in this study.

Disclosures. The authors declare no conflicts of interest.

Data Availability. Data underlying the results presented in this paper are available from the authors upon reasonable request.

[†]Co-first authors with equal contribution.

REFERENCES

1. A. Forbes, "Structured light: tailored for purpose," Opt. Photon. News **31**(6), 24–31 (2020).
2. L. Allen, M. W. Beijersbergen, R. J. C. Spreeuw, and J. P. Woerdman, "Orbital angular momentum of light and the transformation of Laguerre-Gaussian laser modes," Phys. Rev. A **45**, 8185–8189 (1992).
3. A. M. Yao and M. J. Padgett, "Orbital angular momentum: origins, behavior and applications," Adv. Opt. Photon. **3**, 161–204 (2011).
4. Q. Zhan, "Cylindrical vector beams: from mathematical concepts to applications," Adv. Opt. Photon. **1**, 1–57 (2009).
5. A. Holleczek, A. Aiello, C. Gabriel, C. Marquardt, and G. Leuchs, "Classical and quantum properties of cylindrically polarized states of light," Opt. Express **19**, 9714–9736 (2011).
6. G. Gibson, J. Courtial, M. J. Padgett, M. Vasnetsov, V. Pas'ko, S. M. Barnett, and S. Franke-Arnold, "Free-space information transfer using

light beams carrying orbital angular momentum," Opt. Express **12**, 5448–5456 (2004).
7. J. Wang, J. Y. Yang, I. M. Fazal, N. Ahmed, Y. Yan, H. Huang, Y. Ren, Y. Yue, S. Dolinar, M. Tur, and A. E. Willner, "Terabit free-space data transmission employing orbital angular momentum multiplexing," Nat. Photonics **6**, 488–496 (2012).
8. A. E. Willner, H. Huang, Y. Yan, Y. Ren, N. Ahmed, G. Xie, C. Bao, L. Li, Y. Cao, Z. Zhao, J. Wang, M. P. J. Lavery, M. Tur, S. Ramachandran, A. F. Molisch, N. Ashrafi, and S. Ashrafi, "Optical communications using orbital angular momentum beams," Adv. Opt. Photon. **7**, 66–106 (2015).
9. G. Milione, M. P. J. Lavery, H. Huang, Y. Ren, G. Xie, T. A. Nguyen, E. Karimi, L. Marrucci, D. A. Nolan, R. R. Alfano, and A. E. Willner, "4 × 20 Gbit/s mode division multiplexing over free space using vector modes and a q-plate mode (de)multiplexer," Opt. Lett. **40**, 1980–1983 (2015).
10. A. Trichili, C. Rosales-Guzmán, A. Dudley, B. Ndagano, A. Ben Salem, M. Zghal, and A. Forbes, "Optical communication beyond orbital angular momentum," Sci. Rep. **6**, 27674 (2016).
11. A. Mair, A. Vaziri, G. Weihs, and A. Zeilinger, "Entanglement of the orbital angular momentum states of photons," Nature **412**, 313–316 (2016).
12. G. Molina-Terriza, A. Vaziri, J. Řeháček, Z. Hradil, and A. Zeilinger, "Triggered qutrits for quantum communication protocols," Phys. Rev. Lett. **92**, 167903 (2004).
13. R. Fickler, R. Lapkiewicz, W. N. Plick, M. Krenn, C. Schaeff, S. Ramelow, and A. Zeilinger, "Quantum entanglement of high angular momenta," Science **338**, 640–643 (2012).
14. G. Spektor, D. Kilbane, A. K. Mahro, B. Frank, S. Ristok, L. Gal, P. Kahl, D. Podbiel, S. Mathias, H. Giessen, F. J. Meyer Zu Heringdorf, M. Orenstein, and M. Aeschlimann, "Revealing the subfemtosecond dynamics of orbital angular momentum in nanoplasmonic vortices," Science **355**, 1187–1191 (2017).
15. B. Bahari, L. Hsu, S. H. Pan, D. Preece, A. Ndao, A. El Amili, Y. Fainman, and B. Kanté, "Photonic quantum Hall effect and multiplexed light sources of large orbital angular momenta," Nat. Phys. **17**, 700–703 (2021).
16. R. Dorn, S. Quabis, and G. Leuchs, "Sharper focus for a radially polarized light beam," Phys. Rev. Lett. **91**, 233901 (2003).
17. S. W. Hell and J. Wichmann, "Breaking the diffraction resolution limit by stimulated emission: stimulated-emission-depletion fluorescence microscopy," Opt. Lett. **19**, 780–782 (1994).
18. M. A. Lauterbach, M. Guillon, A. Soltani, and V. Emiliani, "STED microscope with spiral phase contrast," Sci. Rep. **3**, 2050 (2013).
19. G. Vicidomini, P. Bianchini, and A. Diaspro, "STED super-resolved microscopy," Nat. Methods **15**, 173–182 (2018).
20. C. Guclu, M. Veysi, and F. Capolino, "Photoinduced magnetic nanoprobe excited by an azimuthally polarized vector beam," ACS Photon. **3**, 2049–2058 (2016).
21. H. Fujita and M. Sato, "Nonequilibrium magnetic oscillation with cylindrical vector beams," Sci. Rep. **8**, 15738 (2018).
22. L. Du, A. Yang, A. V. Zayats, and X. Yuan, "Deep-subwavelength features of photonic skyrmions in a confined electromagnetic field with orbital angular momentum," Nat. Phys. **15**, 650–654 (2019).
23. M. Blanco, F. Cambronero, M. T. Flores-Arias, E. Conejero Jarque, L. Plaja, and C. Hernández-García, "Ultraintense femtosecond magnetic nanoprobes induced by azimuthally polarized laser beams," ACS Photon. **6**, 38–42 (2019).
24. V. G. Niziev and A. V. Nesterov, "Influence of beam polarization on laser cutting efficiency," J. Phys. D **32**, 1455–1461 (1999).
25. M. Meier, V. Romano, and T. Feurer, "Material processing with pulsed radially and azimuthally polarized laser radiation," Appl. Phys. A **86**, 329–334 (2007).
26. Y. Jin, O. J. Allegre, W. Perrie, K. Abrams, J. Ouyang, E. Fearon, S. P. Edwardson, and G. Dearden, "Dynamic modulation of spatially structured polarization fields for real-time control of ultrafast laser-material interactions," Opt. Express **21**, 25333–25343 (2013).
27. T. Kuga, Y. Torii, N. Shiokawa, T. Hirano, Y. Shimizu, and H. Sasada, "Novel optical trap of atoms with a doughnut beam," Phys. Rev. Lett. **78**, 4713–4716 (1997).
28. D. G. Grier, "A revolution in optical manipulation," Nature **424**, 810–816 (2003).
29. M. Padgett and R. Bowman, "Tweezers with a twist," Nat. Photonics **5**, 343–348 (2011).
30. A. Turpin, V. Shvedov, C. Hnatovsky, Y. V. Loiko, J. Mompart, and W. Krolikowski, "Optical vault: a reconfigurable bottle beam based on conical refraction of light," Opt. Express **21**, 26335–26340 (2013).
31. Y. Yang, Y.-X. Ren, M. Chen, Y. Arita, and C. Rosales-Guzmán, "Optical trapping with structured light: a review," Adv. Photon. **3**, 034001 (2021).
32. Y. I. Salamin, Z. Harman, and C. H. Keitel, "Direct high-power laser acceleration of ions for medical applications," Phys. Rev. Lett. **100**, 155004 (2008).
33. V. Marceau, C. Varin, T. Brabec, and M. Piché, "Femtosecond 240-keV electron pulses from direct laser acceleration in a low-density gas," Phys. Rev. Lett. **111**, 224801 (2013).
34. A. Picón, A. Benseny, J. Mompart, J. R. Vázquez de Aldana, L. Plaja, G. F. Calvo, and L. Roso, "Transferring orbital and spin angular momenta of light to atoms," New J. Phys. **12**, 083053 (2010).
35. C. T. Schmiegelow, J. Schulz, H. Kaufmann, T. Ruster, U. G. Poschinger, and F. Schmidt-Kaler, "Transfer of optical orbital angular momentum to a bound electron," Nat. Commun. **7**, 12998 (2016).
36. G. De Ninno, J. Wätzel, P. R. Ribič, E. Allaria, M. Coreno, M. B. Danailov, C. David, A. Demidovich, M. Di Fraia, L. Giannessi, K. Hansen, Š. Krušič, M. Manfredda, M. Meyer, A. Mihelič, N. Mirian, O. Plekan, B. Ressel, B. Rösner, A. Simoncig, S. Spampinati, M. Stupar, M. Žitnik, M. Zangrando, C. Callegari, and J. Berakdar, "Photoelectric effect with a twist," Nat. Photonics **14**, 554–558 (2020).
37. S. Sederberg, F. Kong, F. Hufnagel, C. Zhang, E. Karimi, and P. B. Corkum, "Vectorized optoelectronic control and metrology in a semiconductor," Nat. Photonics **14**, 680–685 (2020).
38. A. Niv, G. Biener, V. Kleiner, and E. Hasman, "Manipulation of the Pancharatnam phase in vectorial vortices," Opt. Express **14**, 4208–4220 (2006).
39. S. M. Baumann, D. M. Kalb, L. H. MacMillan, and E. J. Galvez, "Propagation dynamics of optical vortices due to Gouy phase," Opt. Express **17**, 9818–9827 (2009).
40. A. M. Beckley, T. G. Brown, and M. A. Alonso, "Full Poincaré beams," Opt. Express **18**, 10777–10785 (2010).
41. C. H. Yang, Y. Di Chen, S. T. Wu, and A. Y. G. Fuh, "Independent manipulation of topological charges and polarization patterns of optical vortices," Sci. Rep. **6**, 31546 (2016).
42. Y. Zhang, X. Guo, L. Han, P. Li, S. Liu, H. Cheng, and J. Zhao, "Gouy phase induced polarization transition of focused vector vortex beams," Opt. Express **25**, 25725–25733 (2017).
43. M. M. Sánchez-López, J. A. Davis, I. Moreno, A. Cofré, and D. M. Cottrell, "Gouy phase effects on propagation of pure and hybrid vector beams," Opt. Express **27**, 2374–2386 (2019).
44. H. Wang, G. Rui, and Q. Zhan, "Dynamic propagation of optical vortices embedded in full Poincaré beams with rotationally polarization symmetry," Opt. Commun. **351**, 15–25 (2015).
45. X. L. Wang, J. Chen, Y. Li, J. Ding, C. S. Guo, and H. T. Wang, "Optical orbital angular momentum from the curl of polarization," Phys. Rev. Lett. **105**, 253602 (2010).
46. M. V. Berry, "The adiabatic phase and Pancharatnam's phase for polarized light," J. Mod. Opt. **34**, 1401–1407 (1987).
47. D. Zhang, X. Feng, K. Cui, F. Liu, and Y. Huang, "Identifying orbital angular momentum of vectorial vortices with Pancharatnam phase and Stokes parameters," Sci. Rep. **5**, 11983 (2015).
48. K. J. Schafer, B. Yang, L. F. DiMauro, and K. C. Kulander, "Above threshold ionization beyond the high harmonic cutoff," Phys. Rev. Lett. **70**, 1599–1602 (1993).
49. F. Krausz and M. Ivanov, "Attosecond physics," Rev. Mod. Phys. **81**, 163–234 (2009).
50. T. Popmintchev, M. C. Chen, P. Arpin, M. M. Murnane, and H. C. Kapteyn, "The attosecond nonlinear optics of bright coherent X-ray generation," Nat. Photonics **4**, 822–832 (2010).
51. C. Hernández-García, A. Picón, J. San Román, and L. Plaja, "Attosecond extreme ultraviolet vortices from high-order harmonic generation," Phys. Rev. Lett. **111**, 083602 (2013).
52. C. Hernández-García, J. S. Román, L. Plaja, and A. Picón, "Quantum-path signatures in attosecond helical beams driven by optical vortices," New J. Phys. **17**, 093029 (2015).
53. F. Kong, C. Zhang, H. Larocque, Z. Li, F. Bouchard, D. H. Ko, G. G. Brown, A. Korobenko, T. J. Hammond, R. W. Boyd, E. Karimi, and P. B. Corkum, "Vectorizing the spatial structure of high-harmonic radiation from gas," Nat. Commun. **10**, 2020 (2019).
54. J. Wätzel and J. Berakdar, "Topological light fields for highly non-linear charge quantum dynamics and high harmonic generation," Opt. Express **28**, 19469–19481 (2020).

55. J. Wätzel and J. Berakdar, "Multipolar, polarization-shaped high-order harmonic generation by intense vector beams," Phys. Rev. A **101**, 043409 (2020).
56. L. Rego, J. S. Román, A. Picón, L. Plaja, and C. Hernández-García, "Nonperturbative twist in the generation of extreme-ultraviolet vortex beams," Phys. Rev. Lett. **117**, 163202 (2016).
57. R. Géneaux, A. Camper, T. Auguste, O. Gobert, J. Caillat, R. Taïeb, and T. Ruchon, "Synthesis and characterization of attosecond light vortices in the extreme ultraviolet," Nat. Commun. **7**, 12583 (2016).
58. G. Gariepy, J. Leach, K. T. Kim, T. J. Hammond, E. Frumker, R. W. Boyd, and P. B. Corkum, "Creating high-harmonic beams with controlled orbital angular momentum," Phys. Rev. Lett. **113**, 153901 (2014).
59. F. Kong, C. Zhang, F. Bouchard, Z. Li, G. G. Brown, D. H. Ko, T. J. Hammond, L. Arissian, R. W. Boyd, E. Karimi, and P. B. Corkum, "Controlling the orbital angular momentum of high harmonic vortices," Nat. Commun. **8**, 14970 (2017).
60. D. Gauthier, P. R. Ribič, G. Adhikary, A. Camper, C. Chappuis, R. Cucini, L. F. DiMauro, G. Dovillaire, F. Frassetto, R. Géneaux, P. Miotti, L. Poletto, B. Ressel, C. Spezzani, M. Stupar, T. Ruchon, and G. De Ninno, "Tunable orbital angular momentum in high-harmonic generation," Nat. Commun. **8**, 14971 (2017).
61. F. Sanson, A. K. Pandey, F. Harms, G. Dovillaire, E. Baynard, J. Demailly, O. Guilbaud, B. Lucas, O. Neveu, M. Pittman, D. Ros, M. Richardson, E. Johnson, W. Li, P. Balcou, and S. Kazamias, "Hartmann wavefront sensor characterization of a high charge vortex beam in the extreme ultraviolet spectral range," Opt. Lett. **43**, 2780–2783 (2018).
62. L. Rego, K. M. Dorney, N. J. Brooks, Q. L. Nguyen, C.-T. Liao, J. San Román, D. E. Couch, A. Liu, E. Pisanty, M. Lewenstein, L. Plaja, H. C. Kapteyn, M. M. Murnane, and C. Hernández-García, "Generation of extreme-ultraviolet beams with time-varying orbital angular momentum," Science **364**, eaaw9486 (2019).
63. C. Hernández-García, A. Turpin, J. San Román, A. Picón, R. Drevinskas, A. Cerkauskaite, P. G. Kazansky, C. G. Durfee, and Í. J. Sola, "Extreme ultraviolet vector beams driven by infrared lasers," Optica **4**, 520–526 (2017).
64. A. Turpin, L. Rego, A. Picón, J. San Román, and C. Hernández-García, "Extreme ultraviolet fractional orbital angular momentum beams from high harmonic generation," Sci. Rep. **7**, 43888 (2017).
65. W. Paufler, B. Böning, and S. Fritzsche, "Tailored orbital angular momentum in high-order harmonic generation with bicircular Laguerre-Gaussian beams," Phys. Rev. A **98**, 011401 (2018).
66. K. M. Dorney, L. Rego, N. J. Brooks, J. San Román, C.-T. Liao, J. L. Ellis, D. Zusin, C. Gentry, Q. L. Nguyen, J. M. Shaw, A. Picón, L. Plaja, H. C. Kapteyn, M. M. Murnane, and C. Hernández-García, "Controlling the polarization and vortex charge of attosecond high-harmonic beams via simultaneous spin–orbit momentum conservation," Nat. Photonics **13**, 123–130 (2019).
67. E. Pisanty, L. Rego, J. San Román, A. Picón, K. M. Dorney, H. C. Kapteyn, M. M. Murnane, L. Plaja, M. Lewenstein, and C. Hernández-García, "Conservation of Torus-knot angular momentum in high-order harmonic generation," Phys. Rev. Lett. **122**, 203201 (2019).
68. L. Rego, J. San Román, L. Plaja, and C. Hernández-García, "Trains of attosecond pulses structured with time-ordered polarization states," Opt. Lett. **45**, 5636–5639 (2020).
69. E. Meltchakov, C. Hecquet, M. Roulliay, S. De Rossi, Y. Menesguen, A. Jérome, F. Bridou, F. Varniere, M.-F. Ravet-Krill, and F. Delmotte, "Development of Al-based multilayer optics for EUV," Appl. Phys. A **98**, 111–117 (2009).
70. C. Hernández-García, J. A. Pérez-Hernández, J. Ramos, E. C. Jarque, L. Roso, and L. Plaja, "High-order harmonic propagation in gases within the discrete dipole approximation," Phys. Rev. A **82**, 033432 (2010).
71. K.-Y. Chang, L.-C. Huang, K. Asaga, M.-S. Tsai, L. Rego, P.-C. Huang, H. Mashiko, K. Oguri, C. Hernández-García, and M.-C. Chen, "High-order nonlinear dipole response characterized by extreme ultraviolet ellipsometry," Optica **8**, 484–492 (2021).
72. K. S. Budil, P. Salières, M. D. Perry, and A. L'Huillier, "Influence of ellipticity on harmonic generation," Phys. Rev. A **48**, 3437–3440 (1993).
73. M. Lewenstein, P. Balcou, M. Y. Ivanov, A. L'Huillier, and P. B. Corkum, "Theory of high-harmonic generation by low-frequency laser fields," Phys. Rev. A **49**, 2117–2132 (1994).
74. M. J. Padgett and L. Allen, "The Poynting vector in Laguerre-Gaussian laser modes," Opt. Commun. **121**, 36–40 (1995).
75. P. Dietrich, N. H. Burnett, M. Ivanov, and P. B. Corkum, "High-harmonic generation and correlated two-electron multiphoton ionization with elliptically polarized light," Phys. Rev. A **50**, R3585–R3588 (1994).
76. P. Antoine, A. L'Huillier, M. Lewenstein, P. Salières, and B. Carré, "Theory of high-order harmonic generation by an elliptically polarized laser field," Phys. Rev. A **53**, 1725–1745 (1996).
77. E. Pisanty, S. Sukiasyan, and M. Ivanov, "Spin conservation in high-order-harmonic generation using bicircular fields," Phys. Rev. A **90**, 043829 (2014).
78. G. Pariente and F. Quéré, "Spatio-temporal light springs: extended encoding of orbital angular momentum in ultrashort pulses," Opt. Lett. **40**, 2037–2040 (2015).
79. X. Hao, C. Kuang, T. Wang, and X. Liu, "Phase encoding for sharper focus of the azimuthally polarized beam," Opt. Lett. **35**, 3928–3930 (2010).